Nuclear Science and Techniques (2022) 33:163
https://doi.org/10.1007/s41365-022-01146-3

Effects of the momentum dependence of nuclear symmetry potential on pion observables in Sn + Sn collisions at 270 MeV/nucleon

Gao-Feng Wei[1,2] · Xin Huang[1] · Qi-Jun Zhi[1,2] · Ai-Jun Dong[1,2] · Chang-Gen Peng[3] · Zheng-Wen Long[4]

Received: 27 August 2022 / Revised: 27 September 2022 / Accepted: 2 October 2022 / Published online: 12 December 2022

Abstract

Within a transport model, we investigated the effects of the momentum dependence of the nuclear symmetry potential on the pion observables in central Sn + Sn collisions at 270 MeV/nucleon. To this end, the quantity $U_{\rm sym}^{\infty}(\rho_0)$ (i.e., the value of the nuclear symmetry potential at the saturation density ρ_0 and infinitely large nucleon momentum) was used to characterize the momentum dependence of the nuclear symmetry potential. With a certain L (i.e., the slope of the nuclear symmetry energy at ρ_0), the characteristic parameter $U_{\rm sym}^{\infty}(\rho_0)$ of the symmetry potential significantly affects the production of π^- and π^+ and their pion ratios. Moreover, by comparing the charged pion yields, pion ratios, and spectral pion ratios of the theoretical simulations for the reactions ^{108}Sn + ^{112}Sn and ^{132}Sn + ^{124}Sn with the corresponding data in the SπRIT experiments, we found that our results favor a constraint on $U_{\rm sym}^{\infty}(\rho_0)$ (i.e., -160^{+18}_{-9} MeV), and L is also suggested within a range of 62.7 MeV$< L <$ 93.1 MeV. In addition, the pion observable for ^{197}Au + ^{197}Au collisions at 400 MeV/nucleon also supports the extracted value for $U_{\rm sym}^{\infty}(\rho_0)$.

Keywords Nuclear symmetry potential · Momentum dependence · Symmetry energy

1 introduction

The equation of state (EoS) of asymmetric nuclear matter (ANM), especially its nuclear symmetry energy $E_{\rm sym}(\rho)$ term, plays an essential role in studying the structure [1–4] and evolution of radioactive nuclei [5–8], as well as the synthesis of medium and heavy nuclei [9–12]. The $E_{\rm sym}(\rho)$ characterizes the variation in the EoS of the symmetric nuclear matter (SNM) to that of the pure neutron matter (PNM); the latter is closely connected to the neutron star (NS) matter. Naturally, the properties of NS, such as the radius and the deformation of the NS merger, are also closely related to $E_{\rm sym}(\rho)$, especially at densities of approximately twice the saturation density ρ_0 [13–20]. Nevertheless, knowledge of the $E_{\rm sym}(\rho)$ at suprasaturation densities is still limited, although that around and below ρ_0 [21, 22] as well as the isospin-independent part of EoS for ANM (i.e., EoS of SNM [23–25]) are relatively well determined. Essentially, the EoS of the ANM and its $E_{\rm sym}(\rho)$ term are determined by the nuclear mean field, especially its isovector part (i.e., the symmetry/isovector potential [26, 27]). However, because of the extreme challenge of relatively direct detection of the isovector potential in experiments, one extracted only using the nucleon-nucleus scattering and (p,n) charge-exchange reactions between isobaric analog states limited information of the isovector potential at ρ_0 and parameterized as $U_{\rm sym}(\rho_0, E_{\rm k}) = a - bE_{\rm k}$, where $a \approx 22 - 34$ MeV, $b \approx 0.1 - 0.2$, and $E_{\rm k}$ is limited to no more than 200 MeV [28–30].

This work was supported by the National Natural Science Foundation of China (Nos. 11965008 and 11405128), the Guizhou Provincial Science and Technology Foundation (No. [2020]1Y034), and the PhD-funded project of Guizhou Normal University (No. GZNUD[2018]11).

✉ Gao-Feng Wei
wei.gaofeng@gznu.edu.cn

[1] School of Physics and Electronic Science, Guizhou Normal University, Guiyang 550025, China

[2] Guizhou Provincial Key Laboratory of Radio Astronomy and Data Processing, Guizhou Normal University, Guiyang 550025, China

[3] Guizhou Provincial Key Laboratory of Public Big Data, Guizhou University, Guiyang 550025, China

[4] College of Physics, Guizhou University, Guiyang 550025, China

Heavy-ion collision (HIC) is one of the most promising approaches for exploring the symmetry potential/energy, especially at supersaturation densities [3, 4, 13, 31–33]. Recently, the SπRIT collaboration reported results from the first measurement dedicated to probing the $E_{\rm sym}(\rho)$ at suprasaturation densities through pion production in Sn + Sn collisions at 270 MeV/nucleon carried out at RIKEN-RIBF in Japan [31]. Moreover, they compared the charged pion yields and their single and double pion ratios with the corresponding simulation results from seven transport models. Qualitatively, the theoretical simulations from the seven transport models reach an agreement with the data, yet quantitatively, almost all the models cannot satisfactorily reproduce both the pion yields and their single and double pion ratios of the experimental data [31]. In this situation, author of Ref. [34] claimed that by considering approximately 20% of high-momentum nucleons in colliding nuclei can reproduce both the charged pion yields and their pion ratios of the experimental data quite well because of the high momentum distribution in nuclei caused by short-range correlations (SRCs) [35–40]. Following this work, we focused on the momentum dependence of the symmetry potential because it plays an important role in probing the high-density behavior of $E_{\rm sym}(\rho)$ [41–43]. In fact, in [31] and in [44–48] of the transport model comparison project, the possible reasons for the unsatisfactory results of the seven models quantitatively fitting the experimental data may be due to different assumptions regarding the mean field potential, pion potential, and the treatment of the Coulomb field. Therefore, exploring how the momentum dependence of the symmetry potential affects the pion production in HICs is necessary. Regarding the other aforementioned factors, we also provide detailed considerations based on sophisticated treatment methods, as discussed in Sect. 2. In Sect. 3, we discuss the results of the present study. Finally, a summary is presented in Sect. 4.

2 The model

This study was carried out using an isospin- and momentum-dependent Boltzmann-Uehling-Uhlenbeck (IBUU) transport model. In the framework, the present model is originated from IBUU04 [49, 50] and/or IBUU11 [51] models. However, the present model has been greatly improved to accurately simulate pion production, as discussed below.

First, a separate density-dependent scenario for in-medium nucleon–nucleon interaction [52–54] is expressed as

$$v_D = t_0(1 + x_0P_\sigma)[\rho_{\tau i}(\mathbf{r}_i) + \rho_{\tau j}(\mathbf{r}_j)]^\alpha \delta(\mathbf{r}_{ij}), \tag{1}$$

this equation is used to replace the density-dependent term of the original Gogny effective interaction [55], which is given by

$$\begin{aligned} v(r) = &\sum_{i=1,2}(W + BP_\sigma - HP_\tau - MP_\sigma P_\tau)_i e^{-r^2/\mu_i^2} \\ &+ t_0(1 + x_0P_\sigma)[\rho(\frac{\mathbf{r}_i + \mathbf{r}_j}{2})]^\alpha \delta(\mathbf{r}_{ij}), \end{aligned} \tag{2}$$

where W, B, H, M, and μ are the five parameters, P_τ and P_σ are the isospin and spin exchange operators, respectively, and α is the density-dependent parameter used to mimic the medium effects of many-body interactions [52–54]. As indicated in Ref. [56], the separate density dependence of the effective two-body interactions originates from the renormalization of the multibody force effects, and the latter may extend the density dependence of the effective interactions for calculations beyond the mean field approximation. Moreover, nuclear structure studies have shown that, with the separate density-dependent scenario for the in-medium nucleon–nucleon interaction, more satisfactory results (e.g., the binding energies, single-particle energies, and electron scattering cross sections for ^{16}O, ^{40}Ca, ^{48}Ca, ^{90}Zr, and ^{208}Pr [57]) can be achieved compared with the corresponding experiments. Correspondingly, the potential energy density for the ANM with this improved momentum-dependent interaction (IMDI) is expressed [53] as

$$\begin{aligned} V(\rho,\delta) = &\frac{A_u(x)\rho_n\rho_p}{\rho_0} + \frac{A_l(x)}{2\rho_0}(\rho_n^2 + \rho_p^2) + \frac{B}{\sigma+1}\frac{\rho^{\sigma+1}}{\rho_0^\sigma} \\ &\times\left\{\frac{1+x}{2}(1-\delta^2) + \frac{1-x}{4}\left[(1+\delta)^{\sigma+1} + (1-\delta)^{\sigma+1}\right]\right\} \\ &+ \frac{1}{\rho_0}\sum_{\tau,\tau'} C_{\tau,\tau'}\int\int d^3p d^3p' \frac{f_\tau(\mathbf{r},\mathbf{p})f_{\tau'}(\mathbf{r},\mathbf{p}')}{1+(\mathbf{p}-\mathbf{p}')^2/\Lambda^2}. \end{aligned} \tag{3}$$

In the mean field approximation, Eq. (3) leads to the following single-nucleon potential for the proposed model [52–54]:

$$\begin{aligned} U(\rho,\delta,\mathbf{p},\tau) = &A_u(x)\frac{\rho_{-\tau}}{\rho_0} + A_l(x)\frac{\rho_\tau}{\rho_0} + \frac{B}{2}\left(\frac{2\rho_\tau}{\rho_0}\right)^\sigma(1-x) \\ &+ \frac{2B}{\sigma+1}\left(\frac{\rho}{\rho_0}\right)^\sigma(1+x)\frac{\rho_{-\tau}}{\rho}\left[1+(\sigma-1)\frac{\rho_\tau}{\rho}\right] \\ &+ \frac{2C_l}{\rho_0}\int d^3p'\frac{f_\tau(\mathbf{p}')}{1+(\mathbf{p}-\mathbf{p}')^2/\Lambda^2} \\ &+ \frac{2C_u}{\rho_0}\int d^3p'\frac{f_{-\tau}(\mathbf{p}')}{1+(\mathbf{p}-\mathbf{p}')^2/\Lambda^2}, \end{aligned} \tag{4}$$

where $\sigma = \alpha + 1$, $\tau = 1$ for neutrons and -1 for protons, and the parameters $A_u(x)$, $A_l(x)$, $C_u(\equiv C_{\tau,-\tau})$ and $C_l(\equiv C_{\tau,\tau})$ are expressed as

$$A_l(x) = A_{l0} + U_{\rm sym}^\infty(\rho_0) - \frac{2B}{\sigma+1} \tag{5}$$

$$\times\left[\frac{(1-x)}{4}\sigma(\sigma+1)-\frac{1+x}{2}\right],$$

$$A_u(x) = A_{u0} - U_{\rm sym}^{\infty}(\rho_0) + \frac{2B}{\sigma+1} \tag{6}$$

$$\times\left[\frac{(1-x)}{4}\sigma(\sigma+1)-\frac{1+x}{2}\right],$$

$$C_l = C_{l0} - 2U_{\rm sym}^{\infty}(\rho_0)\frac{p_{f0}^2}{\Lambda^2 \ln\left[(4p_{f0}^2+\Lambda^2)/\Lambda^2\right]}, \tag{7}$$

$$C_u = C_{u0} + 2U_{\rm sym}^{\infty}(\rho_0)\frac{p_{f0}^2}{\Lambda^2 \ln\left[(4p_{f0}^2+\Lambda^2)/\Lambda^2\right]}, \tag{8}$$

where $p_{\rm f0}$ is the nucleon Fermi momentum in the SNM at ρ_0 and $U_{\rm sym}^{\infty}(\rho_0)$ proposed in [51] and is used to characterize the momentum dependence of the symmetry potential at ρ_0. We also illustrate the derivation of Eqs. (5), (6), (7) and (8) and the expression of the symmetry potential and/or energy (see [53]). Currently, knowledge of the momentum dependence of the symmetry potential even at ρ_0 is limited [28–30]. Therefore, taking the parameterized symmetry potential as a reference, we treat $U_{\rm sym}^{\infty}(\rho_0)$ as a free parameter similar to the x parameter, which is used to mimic the slope value $L \equiv 3\rho(\mathrm{d}E_{\rm sym}/\mathrm{d}\rho)$ of $E_{\rm sym}(\rho)$ at ρ_0 without changing the value of $E_{\rm sym}(\rho)$ at ρ_0 and any properties of the SNM. A similar quantity (i.e., y parameter) in [58–60] has been used to describe the momentum dependence of the symmetry potential at ρ_0; however, its quantitative constraints have not been determined. Additionally, it should be noted that the B terms in Eqs. (3) and (4), as well as in the expressions of A_u and A_l, are different from those in [58–60]. This is because the separate density-dependent scenario for in-medium nucleon–nucleon interaction has been adopted in the present model for a more delicate treatment of the in-medium many-body force effects [53], which significantly affects pion production in HICs [54]. The seven parameters A_{l0}, A_{u0}, B, σ, C_{l0}, C_{u0}, and Λ were determined by fitting seven experimental and/or empirical constraints on the properties of nuclear matter at $\rho_0 = 0.16\ \mathrm{fm}^{-3}$. The first six quantities are the binding energy -16 MeV, pressure $P_0 = 0$ MeV/fm^3, incompressibility $K_0 = 230$ MeV for SNM, isoscalar effective mass $m_s^* = 0.7m$, isoscalar potential at infinitely large nucleon momentum $U_0^{\infty}(\rho_0) = 75$ MeV, and symmetry energy $E_{\rm sym}(\rho_0) = 32.5$ MeV, and the seventh quantity is considered as $U_{\rm sym}^{\infty}(\rho_0)$. The values of these parameters are $A_{l0} = A_{u0} = -66.963$ MeV, $B = 141.963$ MeV, $C_{l0} = -60.486$ MeV, $C_{u0} = -99.702$ MeV, $\sigma = 1.2652$, and $\Lambda = 2.424p_{f0}$.

The upper windows in Fig. 1 show the kinetic energy-dependent neutron and proton potentials at ρ_0 with

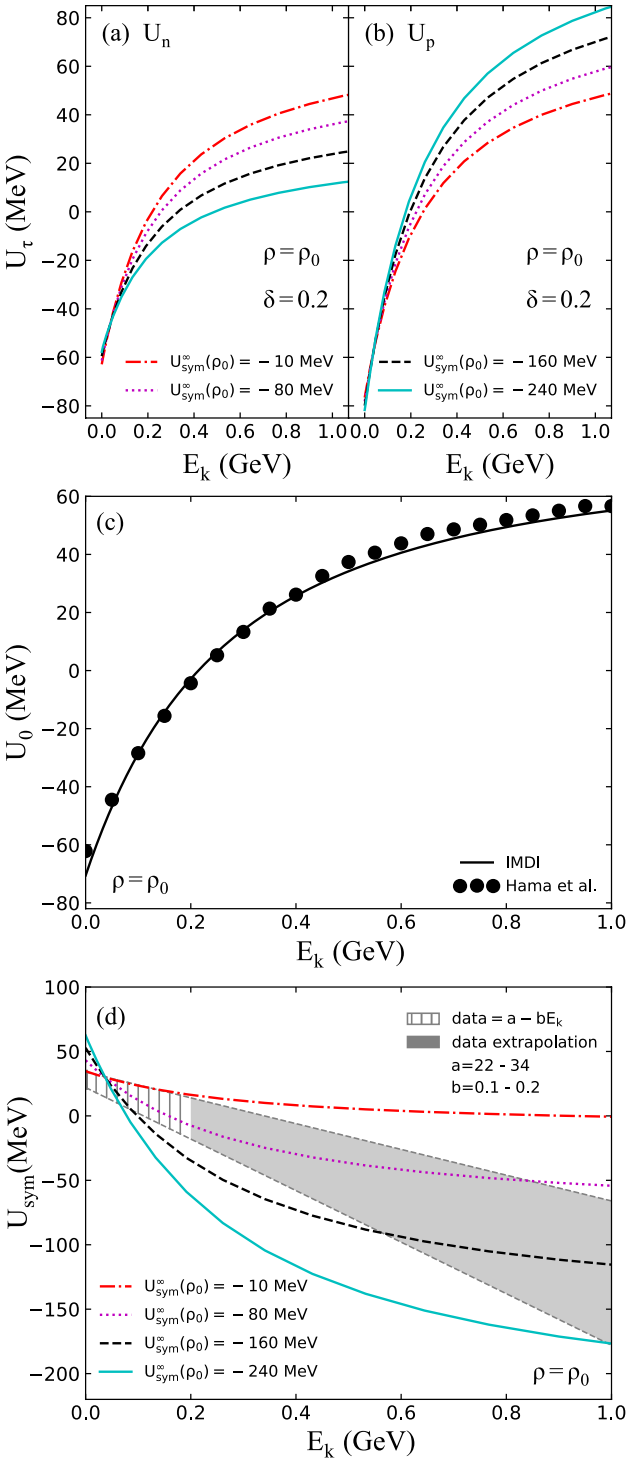

Fig. 1 (Color online) Kinetic energy-dependent neutron **a** and proton **b** potentials as well the isoscalar **c** and isovector **d** potentials at ρ_0 calculated from the IMDI interaction. The Schrödinger-equivalent isoscalar potential obtained by Hama et al. and the parameterized isovector potential from the experimental and/or empirical data are also shown to compare with the isoscalar and isovector potentials calculated from the IMDI interaction

different $U_{\rm sym}^{\infty}(\rho_0)$ values calculated from the IMDI interaction. As $|U_{\rm sym}^{\infty}(\rho_0)|$ increases, the neutron potential shows the opposite variation tendency compared with the proton potential because of the isospin effects. The middle and lower windows in Fig. 1 show the isoscalar and isovector potentials at ρ_0 in comparison with the Schrödinger-equivalent isoscalar potential obtained by Hama et al. [61, 62] and parameterized isovector potentials from experimental and/or empirical data [28–30]. To provide more intuitive references for $U_{\rm sym}^{\infty}(\rho_0)$, we extrapolate the experimental and/or empirical isovector potential to the nucleon kinetic energy up to 1 GeV. Evidently, good consistency can be seen for the isoscalar potential between the present model and that of Hama et al. Moreover, the values of our symmetry potentials at the Fermi kinetic energy (i.e., approximately 36.8 MeV), are the same and within the allowed range of experimental and/or empirical data, even with different $U_{\rm sym}^{\infty}(\rho_0)$. It is based on the values of symmetry potentials at the Fermi kinetic energy and the infinite nucleon momentum that we used to determine the momentum dependence of the symmetry potential at ρ_0. However, because the isoscalar potentials remain unchanged with different $U_{\rm sym}^{\infty}(\rho_0)$, differences in momentum dependence between symmetry potentials with different $U_{\rm sym}^{\infty}(\rho_0)$ are expected to be reflected by the pion observable in HICs because the different symmetry potentials can lead to different isospin effects and thus different π^-/π^+ ratios for neutron-rich reactions. Therefore, to clearly obtain the pion observable, in which the effects of the momentum dependence of the symmetry potentials are reflected, it is useful to map momentum-dependent symmetry potentials with different $U_{\rm sym}^{\infty}(\rho_0)$ into cases with the same $E_{\rm sym}(\rho)$. This is performed by fitting identical constraints for SNM and identical slope parameter L of $E_{\rm sym}(\rho)$ at ρ_0, and the corresponding results are shown in Fig. 2. Even with the same $E_{\rm sym}(\rho)$, the corresponding symmetry potential could be considerably different because the symmetry potentials depend not only on the nucleon density but also on the nucleon momentum or energy.

Second, we also considered the pion potential effects in HICs to accurately simulate pion production in HICs. Specifically, when the pionic momentum is greater than 140 MeV/c, we use the pion potential based on the Δ-hole model of the form adopted in [62]. We adopt the pion potential of the form used in [63–65] when the pionic momentum is lower than 80 MeV/c, whereas for the pionic momentum falling in the range of 80 to 140 MeV/c, an interpolative pion potential constructed in [62] is used. The present pion potential includes the isospin- and momentum-dependent pion s- and p-wave potentials in a nuclear medium, as in [66] (see [62–65]).

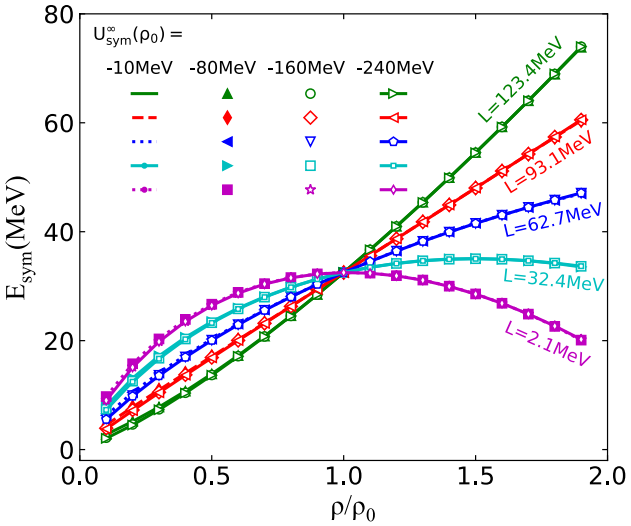

Fig. 2 (Color online) Density dependence of the $E_{\rm sym}(\rho)$ with different $U_{\rm sym}^{\infty}(\rho_0)$ calculated from the IMDI interaction

The in-medium isospin-dependent baryon-baryon elastic and inelastic scattering cross sections $\sigma_{\rm medium}$ are determined by the corresponding free space cross sections $\sigma_{\rm free}$ multiplied by a factor $R_{\rm medium}$, which is expressed as

$$\sigma_{\rm medium} = \sigma_{\rm free} R_{\rm medium}(\rho, \delta, \mathbf{p}), \tag{9}$$

where the reduced factor is determined as $R_{\rm medium} = (\mu_{\rm BB}^*/\mu_{\rm BB})^2$, and $\mu_{\rm BB}$ and $\mu_{\rm BB}^*$ are the reduced masses of the colliding baryon pairs in free space and nuclear medium, respectively.

Finally, for the treatment of the Coulomb field, we calculate the electromagnetic (EM) interactions from the Maxwell equation, that is, $\mathbf{E} = -\nabla\varphi - \partial\mathbf{A}/\partial t$, $\mathbf{B} = \nabla \times \mathbf{A}$, where the scalar potential φ and vector potential $\mathbf{A}$ of the EM fields are calculated from the resources of charges Ze and currents $Ze\mathbf{v}$. For details on EM field effects in HICs, we refer readers to [67–69].

3 Results and discussion

In this section, we focus on the pion production in ^{108}Sn + ^{112}Sn and ^{132}Sn + ^{124}Sn reactions at 270 MeV/nucleon with an impact parameter of $b = 3$ fm. To investigate the sensitivity of pion yields to the high-density behavior of $E_{\rm sym}(\rho)$ (i.e., L) and the momentum dependence of the symmetry potential (i.e., $U_{\rm sym}^{\infty}(\rho_0)$), pion yields are regarded as a function of L for different $U_{\rm sym}^{\infty}(\rho_0)$ values, as shown in Fig. 3. First, consistent with the findings in [34, 70], it is observed that the multiplicities of π^- are more sensitive to L than those of π^+, particularly for the larger isospin asymmetry reactions ^{132}Sn + ^{124}Sn, because π^- is

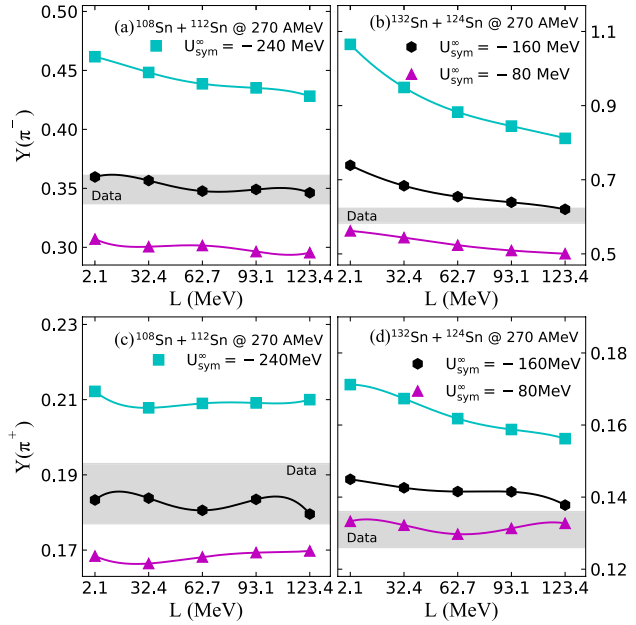

Fig. 3 (Color online) Upper: Multiplicities of π^- generated in reactions ^{108}Sn + ^{112}Sn **a** and ^{132}Sn + ^{124}Sn **b** with different $U^{\infty}_{sym}(\rho_0)$ as a function of L in comparison with the corresponding SπRIT data. Lower: Multiplicities of π^+ generated in reactions ^{108}Sn + ^{112}Sn **c** and ^{132}Sn + ^{124}Sn **d** with different $U^{\infty}_{sym}(\rho_0)$ as a function of L in comparison with the corresponding SπRIT data

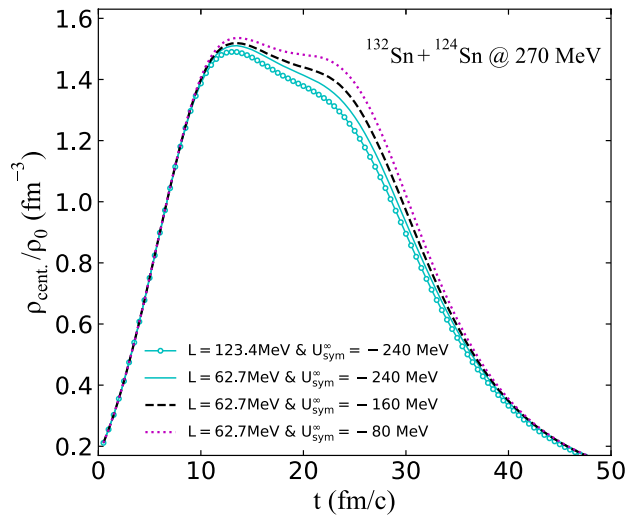

Fig. 4 (Color online) Evolution of the reduced average densities in central region ($\rho_{cent.}/\rho_0$) produced in ^{132}Sn + ^{124}Sn reactions at 270 MeV/nucleon

mostly produced from the neutron–neutron inelastic collisions [70]. Second, with a certain L, the symmetry

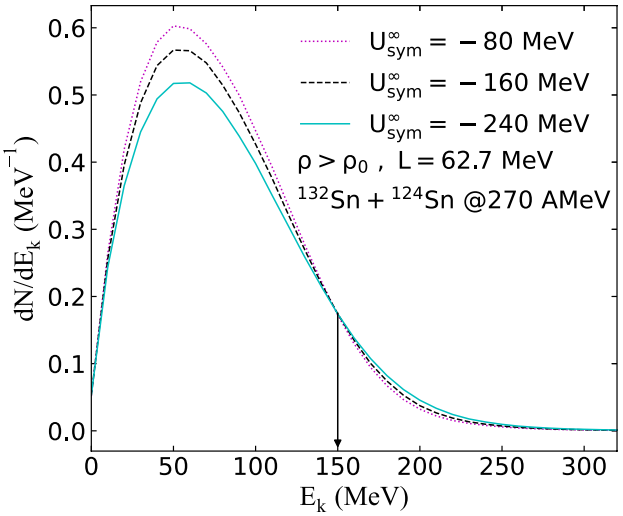

Fig. 5 (Color online) Kinetic energy distribution of nucleons in compression region at $t = 20$ fm/c in ^{132}Sn + ^{124}Sn reactions at 270 MeV/nucleon

potential with a larger value of $|U^{\infty}_{sym}(\rho_0)|$ leads to an increased production of π^- and π^+. To understand this observation, we first check the evolution of the central region densities formed in the HICs. Figure 4 shows the evolutions of the central reduced densities $\rho_{cent.}/\rho_0$ formed in ^{132}Sn + ^{124}Sn reactions with different $U^{\infty}_{sym}(\rho_0)$ but for a certain L of 62.7 MeV. For comparison, we also show the evolution of $\rho_{cent.}/\rho_0$ for the same reaction with $L = 123.4$ MeV and $U^{\infty}_{sym}(\rho_0) = -240$ MeV. With a certain $U^{\infty}_{sym}(\rho_0) = -240$ MeV, the soft symmetry energy with $L = 62.7$ MeV leads to a higher compression compared to that with a stiff symmetry energy $L = 123.4$ MeV, which agrees with previous observations in many studies. Interestingly, we noticed that for a certain $L = 62.7$ MeV, $U^{\infty}_{sym}(\rho_0)$ also affects the evolution of the central region densities. Specifically, approximately at 13 fm/c independent of $U^{\infty}_{sym}(\rho_0)$, the reaction with a certain $L = 62.7$ MeV approaches the maximum compression, generating a maximum compression density $1.5\rho_0$ in the central region; however, the decreasing velocity of this density is slightly faster in the case with a larger $|U^{\infty}_{sym}(\rho_0)|$. This is because the symmetry potential with a larger $|U^{\infty}_{sym}(\rho_0)|$ causes some high-density nucleons to gain more acceleration in the subsequent reaction stages, leading to the densities of the compression region to reduce slightly faster. This can be demonstrated by checking the kinetic energy distribution of the nucleons in the compression region with local densities higher than ρ_0 at $t = 20$ fm/c, as shown in Fig. 5.

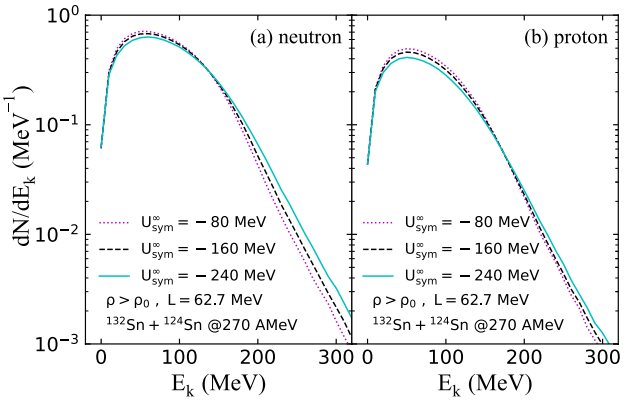

Fig. 6 (Color online) Kinetic energy distribution of neutrons **a** and protons **b** in compression region at $t = 20$ fm/c in ^{132}Sn + ^{124}Sn reactions at 270 MeV/nucleon

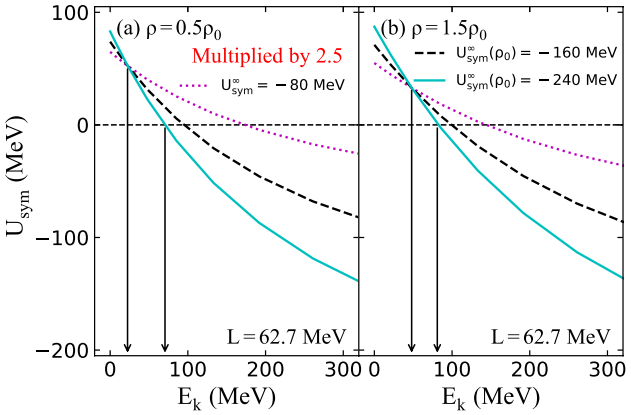

Fig. 7 (Color online) Kinetic energy-dependent symmetry potentials at $\rho = 0.5\rho_0$ **a** and $\rho = 1.5\rho_0$ **b** with different $U^{\infty}_{\rm sym}(\rho_0)$ calculated from the IMDI interaction. The values of symmetry potential at $\rho = 0.5\rho_0$ are multiplied by a factor of 2.5

Clearly, with a certain $L = 62.7$ MeV but varying $U^{\infty}_{\rm sym}(\rho_0)$ from −80 to −240 MeV, we observed increased high-energy nucleons but reduced low-energy nucleons. In general, because the scalar potential has the same repulsive effects on neutrons and protons, whereas the symmetry potential has repulsive (attractive) effects on the high density but low-energy[1] neutrons (protons), these high-energy nucleons might be expected as neutrons. However, as illustrated in Fig. 6, these high-energy nucleons contain both neutrons and protons, and neutrons outnumber protons because the reaction is a neutron-rich system. Moreover, as indicated by the arrows in Fig. 5, the kinetic energies of these energetic neutrons and protons are greater than 150 MeV, whereas the threshold energy of pion production through *NN* inelastic collisions is not more than 300 MeV. Naturally, with a certain L but varying $U^{\infty}_{\rm sym}(\rho_0)$ from −80 to −240 MeV, we can understand the increased production of both π^- and π^+ shown in Fig. 3 because π^- and π^+ are produced mainly from inelastic $nn \to pn\pi^-$ and $pp \to pn\pi^+$ channels. Third, compared with the SπRIT data, as shown in Fig. 3, our prediction of pion multiplicities within a certain range of $U^{\infty}_{\rm sym}(\rho_0)$ can fit the experimental data in general. For the predicted multiplicities, π^+ is not as good as π^-.

To date, one might wonder whether the symmetry potential at $1.5\rho_0$ (i.e., attainable maximum densities in the compression stage) with a certain L but varying $U^{\infty}_{\rm sym}(\rho_0)$ from −80 to −240 MeV could cause both high-energy neutrons and protons to increase. To understand this observation, we illustrate it in the right panel of Fig. 7, which shows the symmetry potential at $1.5\rho_0$ with a certain $L = 62.7$ MeV but different $U^{\infty}_{\rm sym}(\rho_0)$. For completeness, we also demonstrate the corresponding symmetry potential at low densities (i.e., $0.5\rho_0$), as shown in the left panel of Fig. 7. Similar to the symmetry potential at ρ_0, the symmetry potentials at $1.5\rho_0$ even with different $U^{\infty}_{\rm sym}(\rho_0)$ have the same value at approximately the nucleon kinetic energy of 47 MeV. In addition, the value of the symmetry potential also changes from positive to negative when the kinetic energy of the nucleon is larger than a certain value, depending on the value of $U^{\infty}_{\rm sym}(\rho_0)$. Specifically, with a certain $L = 62.7$ MeV but varying $U^{\infty}_{\rm sym}(\rho_0)$ from −80 to −240 MeV, protons (neutrons) in the high-density phase experience stronger attractive (repulsive) effects from the symmetry potentials when their kinetic energies are lower than 47 MeV. In contrast, if their kinetic energies are larger than 47 MeV but lower than approximately 81 MeV[2], protons (neutrons) in the high-density phase will experience more weaker attractive (repulsive) effects from the symmetry potentials. Therefore, with a certain L but varying $U^{\infty}_{\rm sym}(\rho_0)$ from −80 to −240 MeV, the repulsive scalar potential and the weakened attractive symmetry potential can cause some protons to increase their kinetic energies to 150 MeV and above. It should be emphasized that for a reaction with a certain $U^{\infty}_{\rm sym}(\rho_0)$, the effects of L on pion production can be interpreted through the density criterion (i.e., the average maximum densities formed in the reaction compression stages). Nevertheless, for the case with a certain L, interpreting the effects of $U^{\infty}_{\rm sym}(\rho_0)$

[1] Approximately at $t = 13$ fm/c, the reaction approaches maximum compression, the nucleons in compression region are naturally in dense but low-energy phase.

[2] The value of 81 MeV is the transition kinetic energy for the symmetry potential at $1.5\rho_0$ with $L = 62.7$ MeV and $U^{\infty}_{\rm sym}(\rho_0) = -240$ MeV.

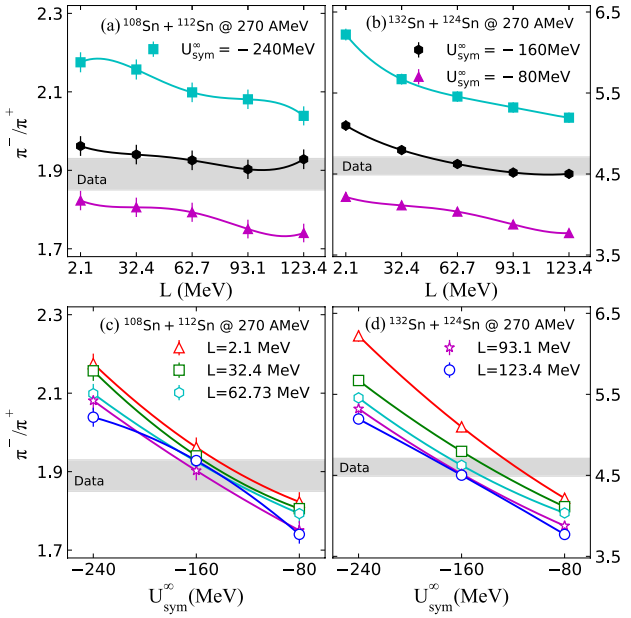

Fig. 8 (Color online) Upper: Ratios of π^-/π^+ generated in reactions ^{108}Sn + ^{112}Sn **a** and ^{132}Sn + ^{124}Sn **b** with different $U^{\infty}_{sym}(\rho_0)$ as a function of L in comparison with the corresponding SπRIT data. Lower: Ratios of π^-/π^+ generated in reactions ^{108}Sn + ^{112}Sn **c** and ^{132}Sn + ^{124}Sn **d** with different L as a function of $U^{\infty}_{sym}(\rho_0)$ in comparison with the corresponding SπRIT data

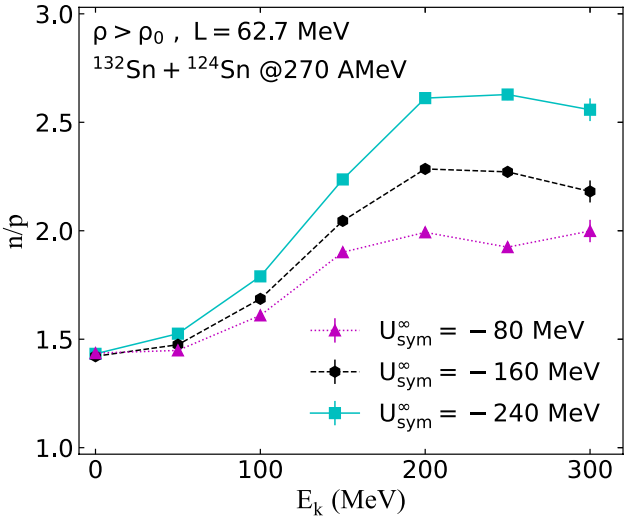

Fig. 9 (Color online) Kinetic energy distribution of neutrons over protons n/p with local densities higher than ρ_0 produced at $t = 20$ fm/c in the reaction ^{132}Sn + ^{124}Sn with different $U^{\infty}_{sym}(\rho_0)$ and a certain L

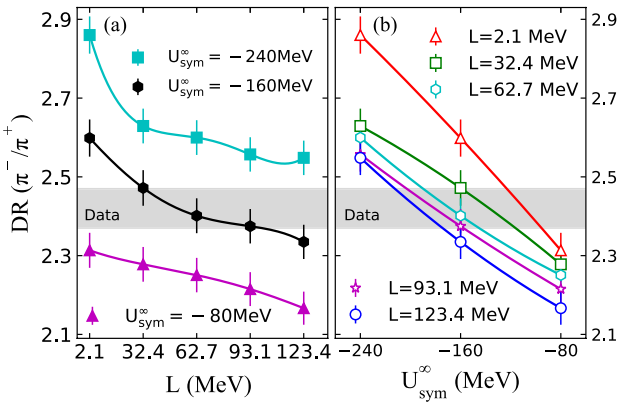

Fig. 10 (Color online) The double π^-/π^+ ratios [i.e., DR(π^-/π^+)] of the reactions ^{132}Sn + ^{124}Sn over ^{108}Sn + ^{112}Sn with different $U^{\infty}_{sym}(\rho_0)$ as a function of L **a** and different L as a function of $U^{\infty}_{sym}(\rho_0)$ **b** in comparison with the corresponding SπRIT data

on pion production requires both density and energy criteria because a small reduction in the average maximum densities formed in the reaction compression stages but a significant increase in the kinetic energy for these high-density nucleons could also lead to increased production of pions.

Figure 8 shows the π^-/π^+ ratios of the theoretical simulations for the same reactions in comparison with SπRIT data. First, consistent with the observations of most transport models, the upper windows of Fig. 8 show that the π^-/π^+ ratios are indeed more sensitive to L than the pion yields, and a softer symmetry energy with a smaller L value leads to a higher π^-/π^+ ratio. Moreover, for a more neutron-rich reaction ^{132}Sn + ^{124}Sn, the π^-/π^+ ratios show a greater sensitivity to L. Second, from the lower windows in Fig. 8, the π^-/π^+ ratios increase with $|U^{\infty}_{sym}(\rho_0)|$ for a certain L. Similar with the reason for more pion production, this observation can also be understood by examining the kinetic energy distribution of neutrons over protons n/p with local densities higher than ρ_0 at $t = 20$ fm/c in reactions ^{132}Sn + ^{124}Sn with a certain L, as shown in Fig. 9. It is observed that with a certain $L = 62.7$ MeV, the ratio n/p increases as $U^{\infty}_{sym}(\rho_0)$ increases from −80 to −240 MeV, because the increment of high-energy neutrons is larger than that of protons for neutron-rich reactions. For this reason, we can observe that for a certain L the π^-/π^+ ratios increase with the value of $|U^{\infty}_{sym}(\rho_0)|$ as shown in Fig. 8. In addition, compared with the SπRIT data, our results for π^-/π^+ ratios also fit the experimental data quite well within a certain range for the value of $U^{\infty}_{sym}(\rho_0)$.

As a cleaner observable, the double ratio of the two reactions (i.e., the DR(π^-/π^+) ratio of reactions ^{132}Sn + ^{124}Sn over ^{108}Sn + ^{112}Sn) has the advantage of reducing both the isoscalar potential effects and the Coulomb field effects; thus, it is expected to disentangle the effects of symmetry potential/energy from both isoscalar potentials and Coulomb fields in HICs. Therefore, in Fig. 10, we show the DR(π^-/π^+) ratios of the two reactions in

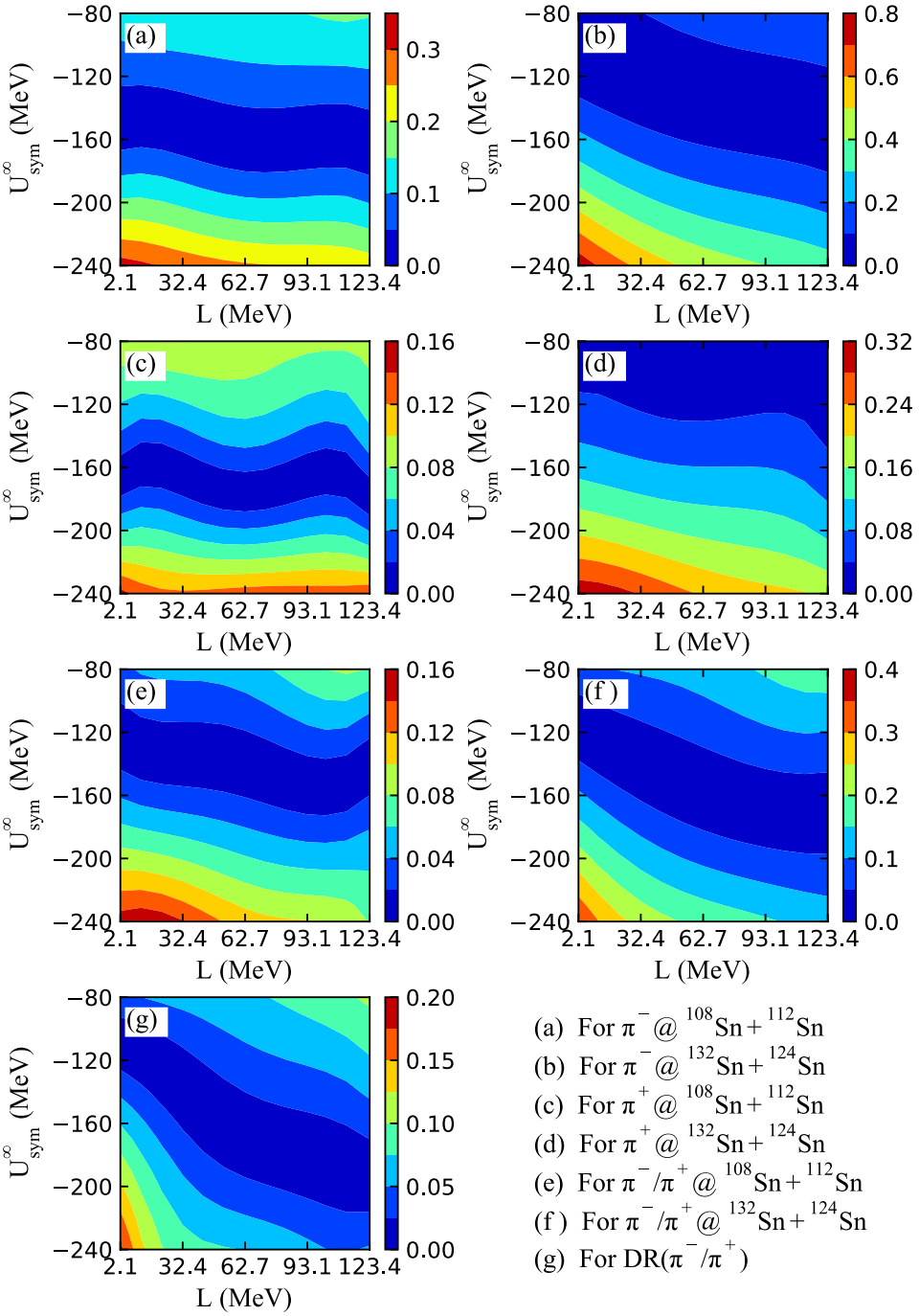

Fig. 11 (Color online) Contours of the relative errors for pion yields and their single and double pion ratios as a function of L and $U^{\infty}_{sym}(\rho_0)$ in reactions ^{108}Sn + ^{112}Sn and ^{132}Sn + ^{124}Sn

comparison with SπRIT data. The left panel of Fig. 10 shows that the DR(π^-/π^+) ratios of the two reactions are more sensitive to the high-density behavior of $E_{sym}(\rho)$. Moreover, the DR(π^-/π^+) ratios are also more clearly separated by varying the value of $U^{\infty}_{sym}(\rho_0)$ from -80 to -240 MeV, making them more sensitive to the momentum dependence of the symmetry potential, as shown in the right panel of Fig. 10.

Now, we attempted to use the above three observables (i.e., pion yields and their single π^-/π^+ and double DR(π^-/π^+) ratios) to constrain the values of $U^{\infty}_{sym}(\rho_0)$ and L. To this end, we perform systematic error analyses for pion yields and their single π^-/π^+ and double DR(π^-/π^+) ratios at different $U^{\infty}_{sym}(\rho_0)$ and L. Apart from pion yields as well as their single π^-/π^+ and double DR(π^-/π^+) ratios at $U^{\infty}_{sym}(\rho_0) = -80, -160$ and -240 MeV and $L = 2.1$, 32.4, 62.7, 93.1, and 123.4 MeV, the values of these observables

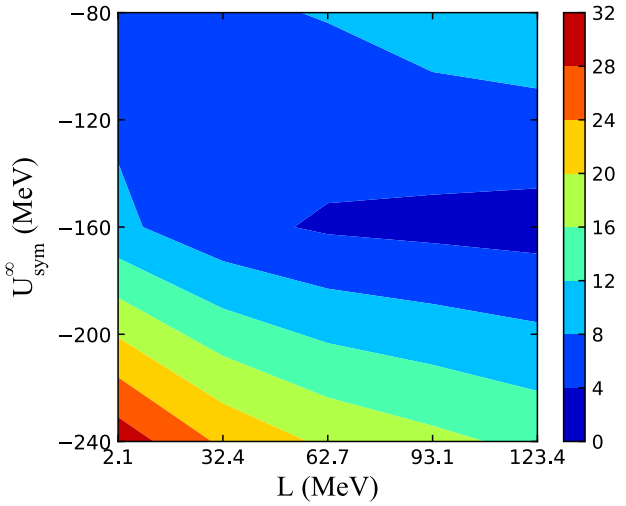

Fig. 12 (Color online) The value of χ as a two-dimensional function of $U^{\infty}_{\rm sym}(\rho_0)$ and L in reactions ^{108}Sn + ^{112}Sn and ^{132}Sn + ^{124}Sn

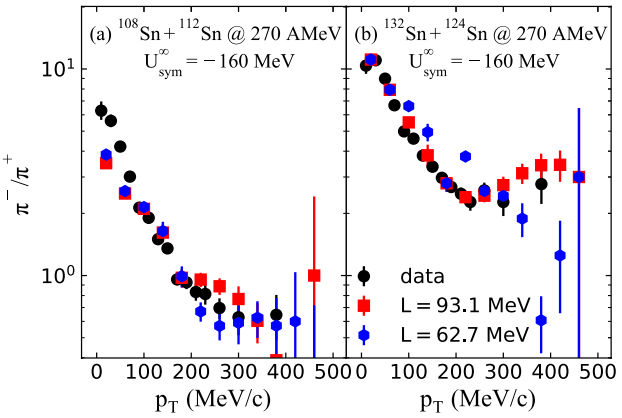

Fig. 13 (Color online) The spectral pion ratios of theoretical simulations for the reactions ^{108}Sn + ^{112}Sn **a** and ^{132}Sn + ^{124}Sn **b** as a function of transverse momentum in comparison with the corresponding data

at other $U^{\infty}_{\rm sym}(\rho_0)$ and L with an interval of 10 MeV are obtained by interpolating the simulation ones. As shown in Fig. 11, the contours of the relative error are the two-dimensional function of L and $U^{\infty}_{\rm sym}(\rho_0)$. However, it is difficult to constrain the values of L and $U^{\infty}_{\rm sym}(\rho_0)$ simultaneously from the relative errors between the theoretical simulations and experimental data. Therefore, we further performed systematic χ−square analyses for these observables at different L and $U^{\infty}_{\rm sym}(\rho_0)$, and the corresponding χ values as a two-dimensional function of L and $U^{\infty}_{\rm sym}(\rho_0)$ are shown in Fig. 12. It is observed that there is an area with

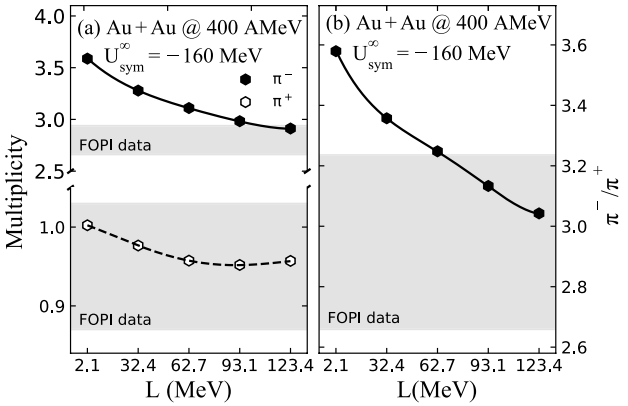

Fig. 14 (Color online) Multiplicities of charged pions **a** and their pion ratios **b** in ^{197}Au + ^{197}Au collisions at 400 MeV/nucleonin comparison with the corresponding data

the highest confidence, in which $U^{\infty}_{\rm sym}(\rho_0)$ is constrained to -160^{+18}_{-9} MeV, and the lower limit of L is approximately no less than 55 MeV.

To further verify the above results, we select a value of −160 MeV for $U^{\infty}_{\rm sym}(\rho_0)$ to check the spectral pion ratios of the reactions ^{108}Sn + ^{112}Sn and ^{132}Sn + ^{124}Sn because this observable, especially its high-energy parts, might be the best probe for the high-density behavior of $E_{\rm sym}(\rho)$, as shown in [13, 48]. Figure 13 shows the spectral pion ratios of the theoretical simulations in comparison with the corresponding data [13]. With this value for $U^{\infty}_{\rm sym}(\rho_0)$, the spectral pion ratios of our simulations, especially its high-energy parts, can fit fairly the experimental data when L ranges from 62.7 to 93.1 MeV. In addition, the pion observable in ^{197}Au + ^{197}Au collisions at 400 MeV/nucleon also supports this value for $U^{\infty}_{\rm sym}(\rho_0)$, as shown in Fig. 14. On the other hand, isospin splitting of the in-medium nucleon effective mass is resulting from the momentum dependence of the symmetry potential. Therefore, it is useful to evaluate the isospin splitting of the in-medium nucleon effective mass for $U^{\infty}_{\rm sym}(\rho_0)$. Based on the formula for the nucleon effective mass

$$m^*_\tau/m = \left[1 + \frac{m}{k_\tau}\frac{dU_\tau}{dk}\right]^{-1}, \tag{10}$$

for the used $U^{\infty}_{\rm sym}(\rho_0) = -10, -80, -160$, and -240 MeV, the corresponding neutron-proton effective mass splittings $\Delta m^*_{\rm np}$ are 0.178δ, 0.384δ, 0.622δ, and 0.864δ, respectively.

So far, one can find that our results suggest a constraint on L (i.e., $62.7 < L < 93.1$ MeV). This constraint on L is considerably close to the values $70 < L < 101$ MeV extracted from charge-exchange and elastic scattering reactions in [71] and within the constrained range of $42 < L < 117$ MeV in [13]. Moreover, our results also suggest a constraint on $U^{\infty}_{\rm sym}(\rho_0)$

(i.e., -160^{+18}_{-9} MeV). We also note that our extracted value for $U^{\infty}_{\rm sym}(\rho_0)$, for example, −160MeV, leads to a larger isospin splitting than the upper limit of 0.33δ in [13, 60]. There may be two reasons for this. First, authors of Ref. [13] used a more accurate criterion (i.e., $E_{\rm sym}(2\rho_0/3) = 25.5$ MeV [72]), and thus considered the uncertainties of $E_{\rm sym}(\rho_0)$ (i.e., 32.5 MeV< $E_{\rm sym}(\rho_0) <$ 38.1 MeV). In this study, we use a fixed value 32.5 MeV for $E_{\rm sym}(\rho_0)$ as commonly used, and thus do not consider its uncertainties. Second, as the separate density-dependent scenario for in-medium nucleon–nucleon interaction has been used in this study, the corresponding potential energy density and single-nucleon potential in Eqs. (3) and (4) and the corresponding expressions for A_l and A_u are different from those in [60]. These two aspects might be the reason for the difference between our extracted isospin splitting and that in [13, 60]. As indicated in [73, 74], the accurate inclusion of these effects might be important for transport model simulations, which may further improve our results (e.g., the deviations of the simulated π^+ from the corresponding data).

Finally, it should be mentioned that our results in the present work are mainly based on SπRIT experiments. It will also be interesting to see how $U^{\infty}_{\rm sym}(\rho_0)$ affects observables measured in other experiments, such as FOPI experiments [33] and ASY-EOS experiments [75].

4 Summary

In conclusion, we studied the effects of the momentum dependence of the symmetry potential on pion production in central Sn + Sn collisions at 270 MeV/nucleon. It was found that with a certain L, the characteristic parameter $U^{\infty}_{\rm sym}(\rho_0)$ of the momentum-dependent symmetry potential significantly affected the production of π^- and π^+ and their pion ratios. Moreover, by performing systematic analyses of these observables and comparing the spectral pion ratios of theoretical simulations with the experimental data, we found a constraint on L (i.e., $62.7 < L < 93.1$ MeV). In addition, $U^{\infty}_{\rm sym}(\rho_0)$ was constrained to -160^{+18}_{-9} MeV. Moreover, the pion observable for ^{197}Au + ^{197}Au collisions at 400 MeV/nucleon supported the extracted value for $U^{\infty}_{\rm sym}(\rho_0)$.

Acknowledgements Gao-Feng Wei would like to thank Profs. Bao-An Li and Gao-Chan Yong for their helpful discussions.

Author Contributions All authors contributed to the study conception and design. Material preparation, data collection and analysis were performed by Gao-Feng Wei, Xin Huang and Qi-Jun Zhi. The first draft of the manuscript was written by Gao-Feng Wei, and all authors commented on previous versions of the manuscript. All authors read and approved the final manuscript.

References

1. S. Typel, B.A. Brown, Neutron radii and the neutron equation of state in relativistic models. Phys. Rev. C **64**, 027302 (2001). https://doi.org/10.1103/PhysRevC.64.027302
2. E.E. Kolomeitsev, C. Hartnack, H.W. Barz et al., Transport theories for heavy-ion collisions in the 1 A GeV regime. J. Phys. G Nucl. Part. Phys. **31**, S741 (2005). https://doi.org/10.1088/0954-3899/31/6/015
3. V. Baran, M. Colonna, V. Greco et al., Reaction dynamics with exotic nuclei. Phys. Rep. **410**, 335 (2005). https://doi.org/10.1016/j.physrep.2004.12.004
4. B.A. Li, L.W. Chen, C.M. Ko, Recent progress and new challenges in isospin physics with heavy-ion reactions. Phys. Rep. **464**, 113 (2008). https://doi.org/10.1016/j.physrep.2008.04.005
5. A. Tamii, I. Poltoratska, P. vonNeumann-Cosel et al., Complete electric dipole response and the neutron skin in ^{208}Pb. Phys. Rev. Lett. **107**, 062502 (2011). https://doi.org/10.1103/PhysRevLett.107.062502
6. X. Viñas, M. Centelles, X. Roca-Maza et al., Density dependence of the symmetry energy from neutron skin thickness in finite nuclei. Eur. Phys. J. A **50**, 27 (2014). https://doi.org/10.1140/epja/i2014-14027-8
7. C.J. Horowitz, E.F. Brown, Y. Kim et al., A way forward in the study of the symmetry energy: experiment, theory, and observation. J. Phys. G Nucl. Part. Phys. **41**, 093001 (2014). https://doi.org/10.1088/0954-3899/41/9/093001
8. P.G. Reinhard, W. Nazarewicz, Nuclear charge and neutron radii and nuclear matter: trend analysis in Skyrme density-functional-theory approach. Phys. Rev. C **93**, 051303 (2016). https://doi.org/10.1103/PhysRevC.93.051303
9. M. Baldo, G.F. Burgio, The nuclear symmetry energy. Prog. Part. Nucl. Phys. **91**, 203 (2016). https://doi.org/10.1016/j.ppnp.2016.06.006
10. C.W. Ma, Y.G. Ma, Shannon information entropy in heavy-ion collisions. Prog. Part. Nucl. Phys. **99**, 120 (2018). https://doi.org/10.1016/j.ppnp.2018.01.002
11. H. Yu, D.Q. Fang, Y.G. Ma, Investigation of the symmetry energy of nuclear matter using isospin-dependent quantum molecular dynamics. Nucl. Sci. Tech. **31**, 61 (2020). https://doi.org/10.1007/s41365-020-00766-x
12. C.W. Ma, H.L. Wei, X.Q. Liu et al., Nuclear fragments in projectile fragmentation reactions. Prog. Part. Nucl. Phys. **121**, 103911 (2021). https://doi.org/10.1016/j.ppnp.2021.103911
13. J. Estee, W.G. Lynch, C.Y. Tsang et al., Probing the symmetry energy with the spectral pion ratio. Phys. Rev. Lett. **126**, 162701 (2021). https://doi.org/10.1103/PhysRevLett.126.162701
14. C.Y. Tsang, M.B. Tsang, P. Danielewicz et al., Insights on Skyrme parameters from GW170817. Phys. Lett. B **796**, 1 (2019). https://doi.org/10.1016/j.physletb.2019.05.055
15. Y. Lim, J.W. Holt, Neutron star tidal deformabilities constrained by nuclear theory and experiment. Phys. Rev. Lett. **121**, 062701 (2018). https://doi.org/10.1103/PhysRevLett.121.062701
16. I. Tews, J. Margueron, S. Reddy, Critical examination of constraints on the equation of state of dense matter obtained from GW170817. Phys. Rev. C **98**, 045804 (2018). https://doi.org/10.1103/PhysRevC.98.045804
17. A. Drago, A. Lavagno, G. Pagliara et al., Early appearance of Δ isobars in neutron stars. Phys. Rev. C **90**, 065809 (2014). https://doi.org/10.1103/PhysRevC.90.065809
18. A.W. Steiner, S. Gandolfi, Connecting neutron star observations to three-body forces in neutron matter and to the nuclear symmetry energy. Phys. Rev. Lett. **108**, 081102 (2012). https://doi.org/10.1103/PhysRevLett.108.081102

19. C. Ducoin, J. Margueron, C. Providência et al., Core-crust transition in neutron stars: Predictivity of density developments. Phys. Rev. C **83**, 045810 (2011). https://doi.org/10.1103/PhysRevC.83.045810
20. J.M. Lattimer, M. Prakash, The equation of state of hot, dense matter and neutron stars. Phys. Rep. **621**, 127 (2016). https://doi.org/10.1016/j.physrep.2015.12.005
21. B.A. Brown, Constraints on the Skyrme equations of state from properties of doubly magic nuclei. Phys. Rev. Lett. **111**, 232502 (2013). https://doi.org/10.1103/PhysRevLett.111.232502
22. B.A. Li, B.J. Cai, L.W. Chen et al., Isospin dependence of nucleon effective masses in neutron-rich matter. Nucl. Sci. Tech. **27**, 141 (2016). https://doi.org/10.1007/s41365-016-0140-4
23. P. Danielewicz, R. Lacey, W.G. Lynch, Determination of the equation of state of dense matter. Science **298**, 1592 (2002). https://doi.org/10.1126/science.1078070
24. M. Oertel, M. Hempel, T. Klahn et al., Equations of state for supernovae and compact stars. Rev. Mod. Phys. **89**, 015007 (2017). https://doi.org/10.1103/RevModPhys.89.015007
25. B.J. Cai, L.W. Chen, Constraints on the skewness coefficient of symmetric nuclear matter within the nonlinear relativistic mean field model. Nucl. Sci. Tech. **28**, 185 (2017). https://doi.org/10.1007/s41365-017-0329-1
26. G.F. Wei, Q.J. Zhi, X.W. Cao et al., Examination of an isospin-dependent single-nucleon momentum distribution for isospin-asymmetric nuclear matter in heavy-ion collisions. Nucl. Sci. Tech. **31**, 71 (2020). https://doi.org/10.1007/s41365-020-00779-6
27. J. Liu, C. Gao, N. Wan et al., Basic quantities of the equation of state in isospin asymmetric nuclear matter. Nucl. Sci. Tech. **32**, 117 (2021). https://doi.org/10.1007/s41365-021-00955-2
28. G.W. Hoffmann, W.R. Coker, Coupled-channel calculations of the energy dependence of the (*p*,*n*) charge-exchange reaction. Phys. Rev. Lett. **29**, 227 (1972). https://doi.org/10.1103/PhysRevLett.29.227
29. A.J. Koning, J.P. Delaroche, Local and global nucleon optical models from 1 KeV to 200 MeV. Nucl. Phys. A **713**, 231 (2003). https://doi.org/10.1016/S0375-9474(02)01321-0
30. J.P. Jeukenne, C. Mahaux, R. Sartor, Dependence of the Fermi energy upon neutron excess. Phys. Rev. C **43**, 2211 (1991). https://doi.org/10.1103/PhysRevC.43.2211
31. G. Jhang, J. Estee, J. Barney et al., Symmetry energy investigation with pion production from Sn+Sn systems. Phys. Lett. B **813**, 136016 (2021). https://doi.org/10.1016/j.physletb.2020.136016
32. R. Shane, A.B. McIntosh, T. Isobe et al., SπRIT: a time-projection chamber for symmetry-energy studies. Nucl. Instr. Meth. A **784**, 513 (2015). https://doi.org/10.1016/j.nima.2015.01.026
33. W. Reisdorf, A. Andronic, R. Averbeck et al., Systematics of central heavy ion collisions in the regime. Nucl. Phys. A **848**, 366 (2010). https://doi.org/10.1016/j.nuclphysa.2010.09.008
34. G.C. Yong, Symmetry energy extracted from the SπRIT pion data in Sn + Sn systems. Phys. Rev. C **104**, 014613 (2021). https://doi.org/10.1103/PhysRevC.104.014613
35. R. Subedi, R. Shneor, P. Monaghan et al., Probing cold dense nuclear matter. Science **320**, 1476 (2008). https://doi.org/10.1126/science.1156675
36. L.B. Weinstein, E. Piasetzky, D.W. Higinbotham et al., Short range correlations and the EMC effect. Phys. Rev. Lett. **106**, 052301 (2011). https://doi.org/10.1103/PhysRevLett.106.052301
37. M.M. Sargsian, New properties of the high-momentum distribution of nucleons in asymmetric nuclei. Phys. Rev. C **89**, 034305 (2014). https://doi.org/10.1103/PhysRevC.89.034305
38. C.C. Degli Atti, In-medium short-range dynamics of nucleons: recent theoretical and experimental advances. Phys. Rep. **590**, 1 (2015). https://doi.org/10.1016/j.physrep.2015.06.002
39. O. Hen, M. Sargsian, L.B. Weinstein et al., Momentum sharing in imbalanced Fermi systems. Science **346**, 614 (2014). https://doi.org/10.1126/science.1256785
40. M. Duer, O. Hen, E. Piasetzky et al., Probing high-momentum protons and neutrons in neutron-rich nuclei. Nature **560**, 617 (2018). https://doi.org/10.1038/s41586-018-0400-z
41. K.A. Brueckner, J. Dabrowski, Symmetry energy and the isotopic spin dependence of the single-particle potential in nuclear matter. Phys. Rev. **134**, B722 (1964). https://doi.org/10.1103/PhysRev.134.B722
42. J. Dabrowski, P. Haensel, Spin and spin-isospin symmetry energy of nuclear matter. Phys. Rev. C **7**, 916 (1973). https://doi.org/10.1103/PhysRevC.7.916
43. V. Giordano, M. Colonna, M.D. Toro et al., Isospin emission and flow at high baryon density: a test of the symmetry potential. Phys. Rev. C **81**, 044611 (2010). https://doi.org/10.1103/PhysRevC.81.044611
44. J. Xu, L.W. Chen, M.B. Tsang et al., Understanding transport simulations of heavy-ion collisions at 100 A and 400 A MeV: comparison of heavy-ion transport codes under controlled conditions. Phys. Rev. C **93**, 044609 (2016). https://doi.org/10.1103/PhysRevC.93.044609
45. Y.X. Zhang, Y.J. Wang, M. Colonna et al., Comparison of heavy-ion transport simulations: collision integral in a box. Phys. Rev. C **97**, 034625 (2018). https://doi.org/10.1103/PhysRevC.97.034625
46. A. Ono, J. Xu, M. Colonna et al., Comparison of heavy-ion transport simulations: collision integral with pions and Δ resonances in a box. Phys. Rev. C **100**, 044617 (2019). https://doi.org/10.1103/PhysRevC.100.044617
47. M. Colonna, Y.X. Zhang, Y.J. Wang et al., Comparison of heavy-ion transport simulations: mean-field dynamics in a box. Phys. Rev. C **104**, 024603 (2021). https://doi.org/10.1103/PhysRevC.104.024603
48. H. Wolter, M. Colonna, D. Cozma et al., Transport model comparison studies of intermediate-energy heavy-ion collisions. Prog. Part. Nucl. Phys. **125**, 103962 (2022). https://doi.org/10.1016/j.ppnp.2022.103962
49. C.B. Das, S. Das Gupta, C. Gale et al., Momentum dependence of symmetry potential in asymmetric nuclear matter for transport model calculations. Phys. Rev. C **67**, 034611 (2003). https://doi.org/10.1103/PhysRevC.67.034611
50. B.A. Li, C.B. Das, S. Das Gupta et al., Momentum dependence of the symmetry potential and nuclear reactions induced by neutron-rich nuclei at RIA. Phys. Rev. C **69**, 011603 (2004). https://doi.org/10.1103/PhysRevC.69.011603
51. L.W. Chen, B.A. Li, *A note of an improved MDI interaction for transport model simulations of heavy ion collisions* (Unpublished, Texas A &M University-Commerce, 2010)
52. C. Xu, B.A. Li, Improved single particle potential for transport model simulations of nuclear reactions induced by rare isotope beams. Phys. Rev. C **81**, 044603 (2010). https://doi.org/10.1103/PhysRevC.81.044603
53. L.W. Chen, C.M. Ko, B.A. Li et al., Probing isospin- and momentum-dependent nuclear effective interactions in neutron-rich matter. Eur. Phys. J. A **50**, 29 (2014). https://doi.org/10.1140/epja/i2014-14029-6
54. G.F. Wei, C. Xu, W. Xie et al., Effects of density-dependent scenarios of in-medium nucleon-nucleon interactions in heavy-ion collisions. Phys. Rev. C **102**, 024614 (2020). https://doi.org/10.1103/PhysRevC.102.024614
55. J. Dechargé, D. Gogny, Hartree-fock-bogolyubov calculations with the D1 effective interaction on spherical nuclei. Phys. Rev. C **21**, 1568 (1980). https://doi.org/10.1103/PhysRevC.21.1568

56. T. Duguet, P. Bonche, Density dependence of two-body interactions for beyond-mean-field calculations. Phys. Rev. C **67**, 054308 (2003). https://doi.org/10.1103/PhysRevC.67.054308
57. J.W. Negele, Structure of finite nuclei in the local-density approximation. Phys. Rev. C **1**, 1260 (1970). https://doi.org/10.1103/PhysRevC.1.1260
58. J. Xu, L.W. Chen, B.A. Li, Thermal properties of asymmetric nuclear matter with an improved isospin- and momentum-dependent interaction. Phys. Rev. C **91**, 014611 (2015). https://doi.org/10.1103/PhysRevC.91.014611
59. H.Y. Kong, Y. Xia, J. Xu et al., Reexamination of the neutron-to-proton-ratio puzzle in intermediate-energy heavy-ion collisions. Phys. Rev. C **91**, 047601 (2015). https://doi.org/10.1103/PhysRevC.91.047601
60. H.Y. Kong, J. Xu, L.W. Chen et al., Constraining simultaneously nuclear symmetry energy and neutron-proton effective mass splitting with nucleus giant resonances using a dynamical approach. Phys. Rev. C **95**, 034324 (2017). https://doi.org/10.1103/PhysRevC.95.034324
61. S. Hama, B.C. Clark, E.D. Cooper et al., Global Dirac optical potentials for elastic proton scattering from heavy nuclei. Phys. Rev. C **41**, 2737 (1990). https://doi.org/10.1103/PhysRevC.41.2737
62. O. Buss, T. Gaitanos, K. Gallmeister et al., Transport-theoretical description of nuclear reactions. Phys. Rep. **512**, 1 (2012). https://doi.org/10.1016/j.physrep.2011.12.001
63. M. Ericson, T.E.O. Ericson, Optical properties of low-energy pions in nuclei. Ann. Phys. **36**, 323 (1966). https://doi.org/10.1016/0003-4916(66)90302-2
64. C. García-Recio, E. Oset, L.L. Salcedo, S-wave optical potential in pionic atoms. Phys. Rev. C **37**, 194 (1988). https://doi.org/10.1103/PhysRevC.37.194
65. J. Nieves, E. Oset, C. García-Recio, Many-body approach to low-energy pion-nucleus scattering. Nucl. Phys. A **554**, 554 (1993). https://doi.org/10.1016/0375-9474(93)90246-T
66. Z. Zhang, C.M. Ko, Medium effects on pion production in heavy ion collisions. Phys. Rev. C **95**, 064604 (2017). https://doi.org/10.1103/PhysRevC.95.064604
67. G.F. Wei, C. Liu, X.W. Cao et al., Necessity of self-consistent calculations for the electromagnetic field in probing the nuclear symmetry energy using pion observables in heavy-ion collisions. Phys. Rev. C **103**, 054607 (2021). https://doi.org/10.1103/PhysRevC.103.054607
68. G.F. Wei, B.A. Li, G.C. Yong et al., Effects of retarded electrical fields on observables sensitive to the high-density behavior of the nuclear symmetry energy in heavy-ion collisions at intermediate energies. Phys. Rev. C **97**, 034620 (2018). https://doi.org/10.1103/PhysRevC.97.034620
69. G.F. Wei, G.C. Yong, L. Ou et al., Beam-energy dependence of the relativistic retardation effects of electrical fields on the π^-/π^+ ratio in heavy-ion collisions. Phys. Rev. C **98**, 024618 (2018). https://doi.org/10.1103/PhysRevC.98.024618
70. B.A. Li, G.C. Yong, W. Zuo, Near-threshold pion production with radioactive beams. Phys. Rev. C **71**, 014608 (2005). https://doi.org/10.1103/PhysRevC.71.014608
71. P. Danielewicz, P. Singh, J. Lee, Symmetry energy III: Isovector skins. Nucl. Phys. A **958**, 147 (2017). https://doi.org/10.1016/j.nuclphysa.2016.11.008
72. M.D. Cozma, Feasibility of constraining the curvature parameter of the symmetry energy using elliptic flow data. Eur. Phys. J. A **54**, 40 (2018). https://doi.org/10.1140/epja/i2018-12470-1
73. Z. Zhang, C.M. Ko, Effects of energy conservation on equilibrium properties of hot asymmetric nuclear matter. Phys. Rev. C **97**, 014610 (2018). https://doi.org/10.1103/PhysRevC.97.014610
74. J.R. Stone, P. Danielewicz, Y. Iwata, Proton and neutron density distributions at supranormal density in low- and medium-energy heavy-ion collisions. Phys. Rev. C **96**, 014612 (2017). https://doi.org/10.1103/PhysRevC.96.014612
75. P. Russotto, S. Gannon, S. Kupny et al., Results of the ASY-EOS experiment at GSI: the symmetry energy at suprasaturation density. Phys. Rev. C **94**, 034608 (2016). https://doi.org/10.1103/PhysRevC.94.034608